

Variable-energy positron-beam studies of Ni implanted with He

K. G. Lynn, D. M. Chen, Bent Nielsen, and R. Pareja
Brookhaven National Laboratory, Upton, New York, 11973

S. Myers

Sandia National Laboratories, Albuquerque, New Mexico 87185

(Received 23 January 1986)

Variable-energy positron-beam studies have been made on well-annealed polycrystalline Ni samples implanted with 30-, 90-, and 180-keV ^4He ions. The positron-annihilation characteristics were measured with a solid-state Ge detector at a number of different incident-positron energies and after isochronal annealing at various temperatures. The Doppler broadening of the annihilation photons was found to be strongly influenced by the ^4He implantations. The data indicate that trapping of the positrons occurred predominantly at small He bubbles. The variation of the broadening with incident-positron energy was sensitive to the depth distribution of the traps. A diffusion model assuming a square concentration-defect profile was developed and analytically fitted to the parametrized momentum data. These fitted results were compared to Monte Carlo range calculations for ^4He in Ni, and fairly good agreement was found. This investigation demonstrates the capabilities of positron annihilation for nondestructive depth profiling in ion-implanted systems. In addition, it establishes parallels between the trapping behavior of positrons and that reported elsewhere for hydrogen, thereby augmenting the present level of understanding of the technologically important trapping of hydrogen by the bubbles.

I. INTRODUCTION

With the development of controllable energy positron beams it is now possible to profile defects, overlayers, and interfaces in the near-surface region ($< 1 \mu\text{m}$) of materials. A few initial studies of this type have been performed by various researchers.^{1,2} We have attempted to semi-quantitatively study the effect of helium implantation on the positron-annihilation characteristics in well-characterized polycrystalline Ni samples.

In the present investigation measurements were made on the annihilation characteristics of low-energy positron beams in Ni following ion implantation of ^4He . This study was motivated by two considerations. First, ion-implanted He in Ni is known to agglomerate into very stable nanometer-sized bubbles, and the depth distribution of these entities can be varied in a known fashion by changing the implantation energy; hence, if such bubbles trap the positrons with an associated observable modification of the annihilation behavior, then specimens of this kind can be used to test the profiling capabilities of the positron analysis. The second objective was to examine in detail the trapping behavior of positrons at the He bubbles, within which the atomic density of the He is believed to be of order 10^{23} (Ref. 3). Such information is expected to enhance the current understanding of the strong hydrogen trapping which often occurs at such bubbles,⁴ an effect with strong relevance to plasma-wall interactions in fusion energy.

To accomplish these goals we implanted monoenergetic positrons into the Ni samples at various energies. After the thermalization (or energy loss) processes ($\lesssim 10$ psec) the implanted positron eventually annihilates with an elec-

tron, producing predominantly two annihilation γ rays.⁵ Measurements of the positron's lifetime, the angular distribution of the annihilation photons, or the Doppler broadening of the γ -ray spectrum provide useful information on the environment of the positron at the time of annihilation. In this experiment the last quantity was studied. To actually profile the implanted region one measures the Doppler spectrum at various incident positron energies. The change from unimplanted Ni is then greatest when the mean range of the positron profile overlaps the He-implanted region.

The Doppler broadening of the γ -ray spectrum is determined by the momentum distribution of the e^+e^- system prior to annihilation. For a perfect crystal the spectrum results from positrons diffusing within the lattice and subsequently annihilating with both conduction and core electrons. In simple metals the Doppler-broadened energy spectrum can be approximated with a central parabolic region representing the conduction-electron contribution superimposed with a broad but smaller core-electron part. If a sample contains open-volume defects, there is a finite probability for positrons to be trapped in these regions. The total electron density as well as the core fraction are reduced at the site of the trapped positron. As a result there is a narrowing of the γ spectrum. The peak height and shape of the resulting Doppler-broadened spectra are different depending on the type of defect where the positron is localized when annihilation occurs. Such a spectrum can be characterized by a line-shape parameter S which simply divides the total spectrum into the central region. This generally provides one with the ability to determine the fraction of positrons which annihilate with these defects. One can also esti-

mate the concentration of defects—if a good estimate can be obtained for the specific trapping rates into these defects. These rates have been theoretically estimated⁶ for simple defects and, in a few cases, have been determined experimentally for different, more complex defects from bulk positron-annihilation studies.⁷ These estimated transition rates into defects are for thermalized positrons; however, with a high defect concentration we find that the transition rate is much higher, an effect which is associated with nonthermal positrons becoming localized into these defects. If a variety of defects are present in the sample and prethermalized trapping occurs, the process of determining the concentration of defects is unlikely without more information.

The ability of positrons to be effectively used for depth profiling of imperfections near surfaces is intimately connected with the knowledge of the positron-implantation profile for a monoenergetic source of positrons. Recently, Monte Carlo calculations⁸ have provided good estimates of this stopping profile; the shape is similar to the derivative of a Gaussian function. One also needs to take account of those positrons which diffuse back to the surface and either escape as positronium (i.e., electron-positron bound state) or suffer inelastic collisions (electron-hole excitations) at the surface and become localized into the image-induced surface state.^{9,10}

This paper will discuss the details of this study in the following order: Section II describes experimental procedures, Sec. III discusses theory and data analysis, Sec. IV presents the results and discussion, and Sec. V covers the conclusion and future prospects. An Appendix is included for a more detailed derivation of the theoretical model used in the theory and data analysis section.

II. EXPERIMENTAL PROCEDURES

The crucial step for the development of this technique was a sufficient flux of energy-moderated positrons. The process of moderation is usually accomplished by choosing a defect-free metal single crystal exhibiting a negative positron work function and locating it next to a positron-emitting source. Those positrons which stop within a diffusion length of the crystal surface ($\approx 10^3$ Å) can diffuse back to the surface before annihilation and be reemitted with an energy characteristic of the positron work function. At the present time the moderator efficiency is 0.1%, which can supply $\approx 10^6$ positrons/sec with standard positron sources.¹¹ These moderated positrons can then be accelerated to a desired energy and implanted in the sample under study.

Our variable-energy positron beam has been described in some detail in previous publications,¹² so only a brief description will be given here. A 100-mCi ⁵⁸Co source was placed next to a W(110) crystal positron moderator.¹¹ The moderated positron beam was guided with a magnetic (≈ 70 G) field through a single $\mathbf{E} \times \mathbf{B}$ positron energy filter. The beam energy was determined by having the source chamber electrically floated to the desired voltage with an accelerator column connecting the target and source. The vacuum in these experiments was $\approx 2 \times 10^{-8}$ Torr. To ensure that the positron beam was incident on the sample at all energies a channel-electron multiplier ar-

ray (CEMA) could be rotated in front of the sample. The beam diameter was measured to be ≈ 4 mm, and it moved by ± 2 mm on the sample as the incident energy was varied.

The polycrystalline Ni foil used for these studies were obtained from Materials Research Corporation, with a nominal purity of 99.995 wt. % (Marz grade). The samples were annealed at 900°C for 14 h and etched before ⁴He implantation. All of the samples were cut from the same 0.005-cm foil to a size of 1 × 1 cm. The implantations were performed at room temperature to fluences of 1×10^{17} , 1.8×10^{17} , and 2.5×10^{17} ⁴He/cm² for the energies 30, 90, and 180 keV, respectively.

The foil samples were mounted on ≈ 0.3 -cm-thick Marz-grade Ni substrates. The substrates were spot-welded to a polycrystalline Ta foil which could be resistively heated. The heavier Ni substrate provided a more homogeneous heat source as well as a flat plate so as not to generate defects by bending the foil during handling. A Chromel-Alumel thermocouple was affixed to the substrate to monitor the temperature during the heat treatments. During the annealing experiments the samples were maintained at each temperature for 40 min when the temperature step was 50°C or 80 min if it was 100°C and then slowly cooled to room temperature before the next set of measurements were initiated. So, in general, the isochronal anneals were such that $\Delta T/t$ was always kept constant. A reference sample cut from the same foil and annealed in the same way was also measured. Other Ni references were measured to check sample variation.

Annihilation spectra containing $\approx 1 \times 10^6$ counts in the peak were taken at various incident energies after each isochronal anneal. The annihilation photopeak was measured with a 20%-efficient intrinsic Ge detector. The instrumental resolution was measured with a ⁷Be source which decays by emitting a 477-keV γ ray. The full width at half maximum was found to be 1.4 keV at this energy. The central region of the γ spectrum was defined from ≈ 510.5 to ≈ 511.5 keV, the total from ≈ 505 to ≈ 515 keV.

III. THEORY

In our model the thermalized positrons are divided into three possible annihilation sites:

- (1) positrons diffusing in the perfect lattice;
- (2) positrons trapped in surface states or emitted from the surface as para-Ps (singlet state) or ortho-Ps (triplet state) (those that are directly reemitted as free positrons are repelled back to the sample by a retarding field);¹³ and
- (3) positrons trapped at defect sites.

The momenta of the annihilating pair at these different sites are different from one another, hence making the associated S parameters potentially distinguishable. It is therefore appropriate to assign one S parameter to each of these groups. Namely, S_s , S_b , and S_d , where the subscripts represent positrons annihilating from the surface, bulk, and defect, respectively. Clearly, these three parameters are all material and temperature dependent. The value of S_d depends on the type of the defect. It is gen-

erally true that

$$S_s \geq S_d > S_b . \quad (1)$$

The observed S parameter, S_{ob} , is the combination of these three parameters, which are assumed to be linearly weighted (see Ref. 13) by the fraction that annihilates at each location F_i ($i \approx s, b, d$), i.e., the fraction of incident positrons ended in the "ith" group. Thus

$$S_{ob} = F_s S_s + F_d S_d + F_b S_b , \quad (2)$$

in which

$$F_s + F_d + F_b = 1 . \quad (3)$$

The constraint (3) can be combined into Eq. (2) to give

$$S_{ob} = S_b + F_s S_{sb} + F_d S_{db} , \quad (4)$$

where

$$S_{sb} = S_s - S_b , \quad (5)$$

and a similar definition holds for S_{db} . Consequently, a defect-free sample ($F_d = 0$) is represented as

$$F_s + F_b = 1 \quad (6)$$

and

$$S_{ob}^{(0)} = S_b + F_s^{(0)} S_{sb} , \quad (7)$$

where the superscript "0" stands for defect free.

Using Eq. (7), one can rewrite Eq. (4) as

$$\Delta S = S_{ob} - S_{ob}^{(0)} , \quad (8)$$

and hence

$$\Delta S = \Delta F_s S_{sb} + F_d S_{db} , \quad (9)$$

where ΔF_s is given by

$$\Delta F_s = F_s - F_s^{(0)} \quad (10)$$

is the difference between the surface fractions of the same sample with and without defects.

Equation (9) is essentially the same as Eq. (4), except that it provides a more sensitive way of detecting the defects and a more physical picture for profiling defects.

Theoretical expressions for the fraction, F_s , F_d , and F_b , can be obtained by employing a one-dimensional diffusion model including defect trapping, for describing the motion of the positron in the solid:^{14,15}

$$D_+ n(x)'' - [\lambda + K(x)]n(x) + p(x) = 0, \quad 0 \leq x \leq \infty \quad (11)$$

where $n(x)$ is the positron density distribution, $p(x)$ is the positron implantation profile, $K(x)$ is the total trapping rate, λ is the bulk annihilation rate, and D_+ is the positron diffusion coefficient. We have implicitly multiplied a unit time constant throughout the equations.

The equations that determine the relative fractions are as follows: (a) diffusion back to the surface,

$$F_s = -J(0) = D_+ \left. \frac{\partial n(x)}{\partial x} \right|_{x=0} ; \quad (12)$$

(b) trapped in the defect sites,

$$F_d = \int_0^\infty K(x)n(x)dx ; \quad (13)$$

(c) annihilation within the bulk,

$$F_b = \int_0^\infty \lambda n(x)dx . \quad (14)$$

The positron density distribution function is therefore the crucial part in extracting these fractions and one needs to solve Eq. (11) with some appropriate boundary conditions. To simplify the problem, the following assumptions are made:

(1) Perfect surface absorption, i.e.,

$$n(0) = 0, \quad n(\infty) = 0 . \quad (15)$$

All positrons that diffuse back to the surface are either trapped in the surface state or reemitted and decay as positronium. One should note that small changes in the surface condition can change S_s , and therefore it is reasonable to adjust S_s so $\Delta S = 0$ at $E = 0$. This does not change any of the physical parameters other than it allows for the surface conditions to vary, during the experiment.

(2) D_+ and λ have the same values as in the defect-free sample. These two coefficients can be obtained from previous measurements. For Ni (Refs. 16 and 17) we set

$$D_+ \simeq 1 \text{ cm}^2/\text{sec}, \quad \lambda = 10^{10} \text{ sec}^{-1} . \quad (16)$$

(3) Recent Monte Carlo simulation⁸ suggested the positron-implantation profile

$$p(x) = -\frac{d}{dx} e^{-(x/x_0)^m} , \quad (17)$$

where $m = 1.9$ and x_0 is associated with the mean implantation depth \bar{x} via a Γ function:

$$x_0 = \bar{x} / \Gamma \left[1 + \frac{1}{m} \right], \quad \bar{x} = (D_+ / \lambda)^{1/2} \left[\frac{E}{E_0} \right]^n , \quad (18)$$

where E_0 and n are experimentally determined parameters. To reduce the computational effort, $m = 2$ will be used instead. This causes only a minor change in the fitted parameters.

(4) Owing to the saturation of positron trapping in the samples (including those positrons which are not completely thermalized before they are trapped) under study (see the following sections) a constant S_d and a square trapping distribution will be assumed; thus

$$K(x) = \begin{cases} K, & x_1 \leq x \leq x_2 \\ 0, & \text{otherwise} \end{cases} \quad (19)$$

where x_1 and x_2 define the positron trapping region and K is the trapping rate in this region. These variables were treated as fitting parameters in the analysis.

Expressions for F_s , F_d , and F_b can be easily derived from Eqs. (11)–(19) in terms of variables E_0 , n , K , x_1 , and x_2 . We derive the full expressions in the Appendix and only rewrite Eqs. (7) and (9) with explicit arguments for the following discussions:

$$S_{ob}^{(0)} = S_b + S_{sb} F_s^{(0)}(E_0, n) , \quad (20)$$

$$\Delta S = S_{sb} \Delta F_s(E_0, n, x_1, x_2, K) + S_{db} F_d(E_0, n, x_1, x_2, K). \quad (21)$$

It is important to note that Eq. (20) allows one to extract values of S_s , S_b , E_0 , and n characterizing a defect-free sample from fitting this expression to the experimental data taken with a well-annealed defect-free sample. These results can be subsequently used to reduce the number of parameters in Eq. (21). Measurements of ΔS parameter along with Eq. (21) should provide values of the remaining parameters S_d , x_1 , x_2 , and K . These parameters can in theory determine the characteristics of defects present in the sample. Thus the defect profile can be determined by using this technique.

We found for the He-implanted samples that the derivative of Gaussian implantation profile fit the data better than the exponential positron-implantation profile. It is important to note that S_{bd} and K are strongly correlated in the fitting analysis.¹⁸ Small variations in S_{bd} correspond to large variations in K for $K \leq 10\lambda_b$, when $K \geq 20\lambda_b$ the dependence of the change in S on the damage in K weakens drastically. We also find that the non-thermal positron-trapping cross section is defect-concentration dependent and can be an order of magnitude larger than that for thermalized positrons. This is expected when one is in a situation where nearly 100% of the positrons become trapped. A lower ^4He fluence would provide a more reliable fit of K , x_1 , and x_2 . The variations of S_{bd} and K are, however, clearly within values that would not change any conclusions made.

IV. RESULTS AND DISCUSSION

The S parameter versus incident-positron energy for the unimplanted Ni sample well annealed at 1100°C is shown in Fig. 1. The solid curve represents a fit using Eq. (20) with $F_s^{(0)}$ given by Eq. (A13); the latter equation corresponds to a positron-implantation profile which is the derivative of a Gaussian, or $m=2$ in Eq. (17). The dashed curve is a fit where Eq. (20) was employed with $F_s^{(0)}$ given by Eq. (A19), corresponding to an exponential profile, for which $m=1$ in Eq. (17). Both of these formulations are seen to provide a good description of the data, as already indicated in the preceding section. The parameters deduced from these fits are shown in Table I. One can observe that E_0 is smaller for the exponential fit

TABLE I. Fitted parameters of Eqs. (20), (A13), and (A19) to the data of the measured S parameter for the defect-free Ni sample.

| Positron implantation profile | E_0 (keV) | n | S_s | S_b |
|----------------------------------|-------------|-----|-------|-------|
| Derivative of Gaussian ($m=2$) | 6.3 | 1.3 | 0.506 | 0.417 |
| Exponential ($m=1$) | 5.5 | 1.6 | 0.503 | 0.414 |

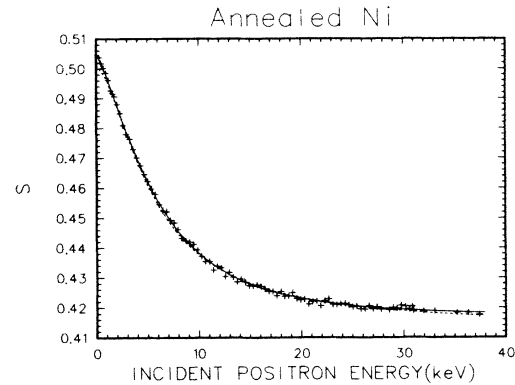


FIG. 1. Measured S parameter as a function of incident-positron energy for an unimplanted Ni sample annealed at 1100°C *in situ*. The solid curve is a fit of Eq. (20) with $F_s^{(0)}$ given by Eq. (A13), corresponding to $m=2$ in Eq. (17); the dashed curve is a fit of Eq. (20) with $F_s^{(0)}$ given by Eq. (A19), corresponding to $m=1$.

which has also been observed and discussed for Si.¹⁹ This is associated with the strong coupling between n and m [Eqs. (17) and (18)]. The values of E_0 determined from this S -parameter measurement are in good agreement with previous positronium-fraction-versus-incident-positron-energy measurements for Ag and Cu.¹⁵ The quantities S_s and S_b each have almost the same fitted value for both profiles, which is expected because they only depend on the material and not the probe profiles. This fact also follows immediately from extrapolating Eqs. (20), (A13), and (A19) to zero or infinite incident-positron energy.

Figure 2 displays the measured S parameter versus incident positron energy for the three He-implanted Ni samples which have been studied. The scatter in the data points is associated with statistical fluctuations and our beam motion. The effects upon the observed S parameters S_{ob} , due to the introduction of open-volume defects via He implantation, are clear. These changes arise from the fact that the annihilation at a defect site produces a larger S parameter than the bulk, i.e., narrower energy peak. As the incident-positron energy is increased, more

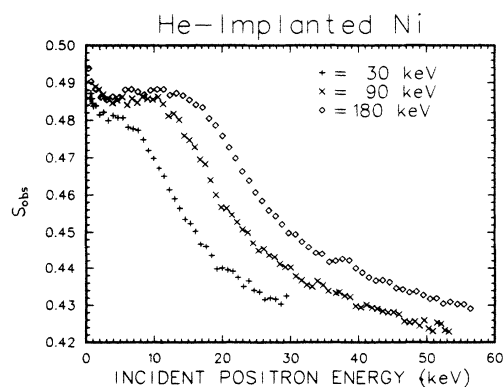


FIG. 2. Observed S parameter versus the incident-positron energy for He-implanted Ni samples with different He-implantation energies as indicated in the figure. Data were taken before heat treatment.

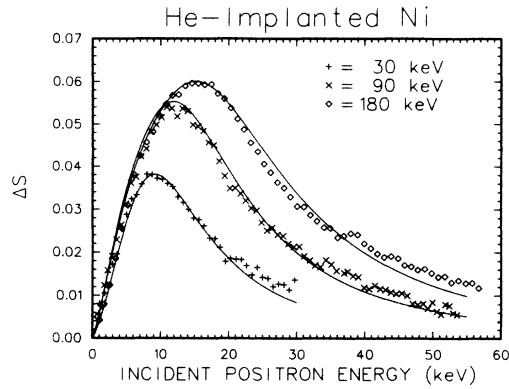


FIG. 3. The difference data obtained by subtracting the fitted curve of the reference data (Fig. 1) from the S_{ob} data (Fig. 2). The solid curves are the results of fitting Eqs. (21) and (A12)–(A14) to each set of the data. The fitted parameters are listed in Table II.

implanted positrons are removed from F_b and F_s and contribute to the fraction trapped in the defects F_d ; as this energy is increased further, positrons are implanted beyond the defect region (F_d decreases), and eventually, at sufficient energy, most of them decay in the bulk region ($F_b \approx 1$) as in the case of the defect-free sample.

To see the consequences of the defects in a more direct way, ΔS data versus incident-positron energy are generated according to Eq. (8) and the result is shown in Fig. 3. An offset is included such that $\Delta S = 0$ at $E = 0$ in these data. If one defines the change as the ratio of ΔS value to the bulk line-shape parameter S_b , the maximum changes in the S parameter were approximately 9%, 13%, and 14.4% for the 30-, 90-, and 180-keV He implantation energies, respectively. The maximum change in the S parameter measured for single vacancies in Ni is approximately 6%.²⁰ This large percentage change measured in the S parameter for these samples compared to vacancy defects is strong evidence that the trapping sites under study are voidlike. As one would expect, the peak positron shifts to increasing positron energy at higher He implantation energy, demonstrating that depth information is definitely present.

Equation (21) was fitted to the data shown in Fig. 3 and the resulting fits are shown as solid curves. The deduced parameters are given in Table II. The parameter m in Eq. (17) for the positron-implantation profile has been set equal to 2, corresponding to the derivative of the Gaussian curve. It also produces more reasonable values for the

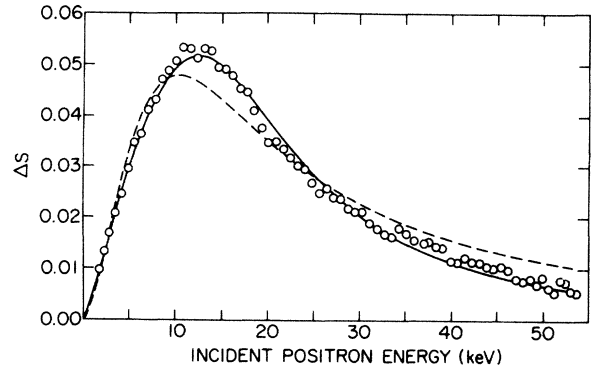


FIG. 4. The difference data of the S parameters for the damage and reference samples and the fitted curves for the 90-keV He-implanted Ni sample. The solid curve is generated using the derivative of a Gaussian ($m = 2$) positron-implantation profile; the dashed curve is generated using the exponential profile ($m = 1$).

deduced parameters (Table II). The agreement between the model and data in Fig. 3 is quite good. The most successful aspect of this simple model is that the fitted trap profiles terminate at the depths where the calculated or damage profiles are well attenuated (Fig. 5). The starting points of these assumed square trap distributions do not correspond as precisely. This may be due in large part to the He tails extending from the surface toward the He peak, caused by the high fluences. The region of complete positron trapping in the present experiment is believed to extend to He concentrations well below those at the peaks.

The positron, ^4He , and damage profile⁵ are displayed on the same depth scale in Fig. 5, in an attempt to provide a physical picture. Figure 5(a) shows the positron-implantation profiles ($m = 2$) of Eq. (17) at the incident-positron energies at which peaks occur in the respective ΔS curves shown in Fig. 3. The rest of the parameters can be found in Table I. The He and damage profiles are obtained from the Monte-Carlo code TRIM (Ref. 21) using 1000 trajectories and are shown in Figs. 5(b) and 5(c). Since trapping by the bubbles is believed to dominate in the present studies, the He distribution is the more relevant one. The average depth of the ^4He implanted at 30, 90, and 180 keV is calculated to be ≈ 1100 , ≈ 2980 , and ≈ 5135 Å, respectively. Taking the simplest plausible picture of the interplay of the positron and He depth distributions in Fig. 5, one might imagine that the peak in ΔS should occur when the overlap integral of the two

TABLE II. Parameters obtained from fitting Eq. (21) and Eqs. (A12)–(A14) to the ΔS data shown in Fig. 3.

| Helium implantation energy (keV) | x_1 (nm) | x_2 (nm) | K [$1/\lambda(\text{psec})$] | S_d |
|----------------------------------|-------------------|------------|----------------------------------|----------|
| 30 | 38^{+245}_{-38} | 220(11) | 20 | 0.492(3) |
| 90 | 125(11) | 401(9) | 20 | 0.492(2) |
| 180 | 113(16) | 596(16) | 25 | 0.491(2) |

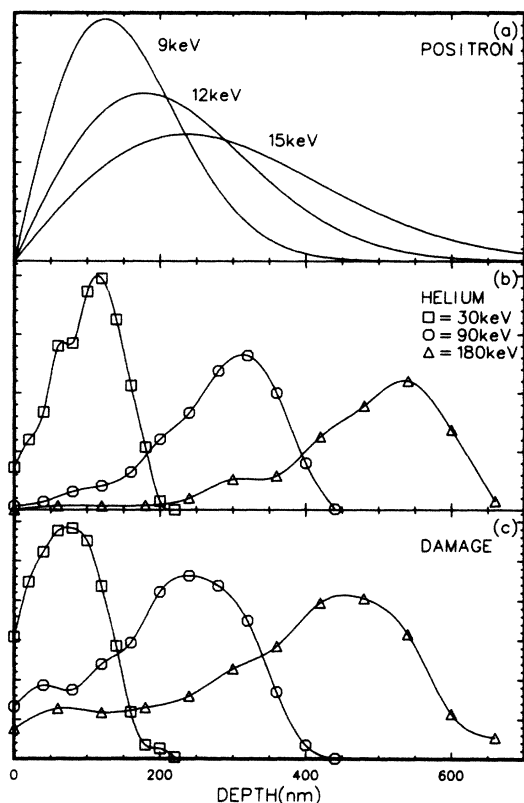


FIG. 5. Calculated (a) positron, (b) He, and (c) implantation-damage profiles. The vertical scales are in arbitrary units. The positron profiles are generated from Eq. (19) with $m = 1.9$, $n = 1.62$, and $E_0 = 6.7$ keV. The selected energies correspond, respectively, to the peak positions of the ΔS curves in Fig. 3. Panels (b) and (c) are results from a TRIM calculation with the different He-implantation energies shown in the legend. The solid curves joining the symbols are the spline interpolation.

functions is maximized. This is not the case, as is evident from comparison of Figs. 3 and 5. The principal reason for this is believed to be the presence of bubbles at densities far exceeding those necessary to trap all of the positrons; as a consequence, the fraction of positrons annihilating within bubbles remains near 100% out into the tails of the He distributions. A second complication is the diffusion of positrons over appreciable distances between the implantation depth and the trap site.

Transmission electron microscopy on the He-implanted Ni sample has shown that following room-temperature implantation²² He had agglomerated into small bubbles about 1 nm in diameter. If we average the He concentration over the fitted depth range (≈ 300 nm) for the 90-keV He-implanted sample and take the He atomic density within the bubbles to be 10^{23} cm⁻³, we find 10^{20} bubbles/cm³, a very high trap concentration. Positrons trapping in monovacancies saturate at a concentration of $\approx 5 \times 10^{15}$ cm⁻³ in most metals. This means that unless there is a very strong competing trap (e.g., surface), all positrons are trapped in bubbles and the fitted values of S_d and K support this. The reason that S is still smaller than S_s for positrons at the surface is due to the high He density and thereby higher local electron density in the

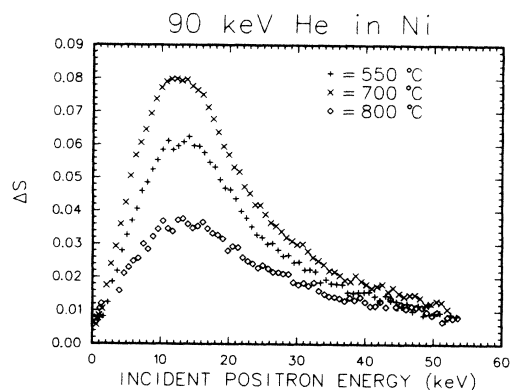


FIG. 6. The difference data of S parameter for the 90-keV He-implanted Ni sample after isochronal annealing up to three different temperatures. Data are obtained in the same manner as for those shown in Fig. 3.

bubbles. This has been demonstrated in Al with high-density He bubbles, where the high electron density caused a strong reduction in the positron lifetime.²³ The reduction was actually used to calculate the pressure in the bubbles. For reference to early bubble nucleation and growth, see Refs. 24 and 25.

Isochronal annealing was performed and followed by additional positron measurements in order to obtain information on the thermal evolution of the traps. Figure 6 shows a typical set of data after three annealing temperatures. Little change has occurred by annealing the sample to 500 °C. This supports the interpretation of positron trapping mainly in bubbles and not other irradiation defects which have been seen with hydrogen.²⁶ Smaller defects would be expected to show recovery in this temperature range. Monovacancies migrate in the temperature range 90–200 °C.^{27,28} Significant increases in ΔS were found by further annealing as can be seen by the 700 and 800 °C data (Fig. 6). Annealing beyond this temperature showed a subsequent decrease in ΔS and is consistent with thermal He release data of Jäger and Roth.²⁹ The thermal He release showed a large change at 800–1000 °C with essentially all of the He released at a temperature of $T_a \approx 1100$ °C.

Figure 7 shows the fitted ΔS peak height versus annealing temperature for the 30-, 90-, and 180-keV ⁴He implant energies. In the temperature range from 500 to 700 °C, a strong increase in ΔS is seen; this is attributed to growth and agglomeration of the bubbles, which reduces the local He density and its associated electron density. One can check that we do have a change in defect type by employing the use of a defect-specific R parameter.³⁰ This parameter is produced by using sections of the momentum spectrum which are unique for different positron traps. One forms a ratio of these momentum regions which uniquely describes a specific defect without being sensitive to changes in defect concentration. We found that when ΔS_{\max} changed we found associated increases in the R parameter. In the temperature range above 700 °C we find a rapid decrease in ΔS and eventually the S value of perfect Ni is obtained, leading to $\Delta S \rightarrow 0$. We interpret this as blistering finally destroying the bubbles. The temperature

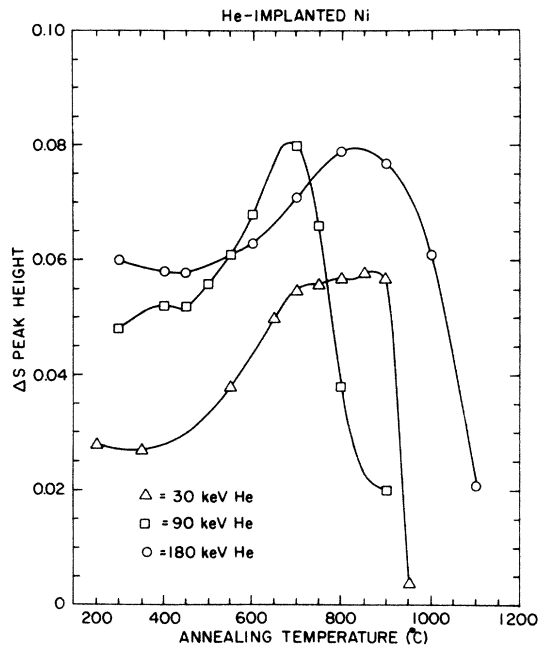


FIG. 7. Peak heights of the ΔS data deduced from measurements after isochronal anneals. The solid curves are the spline-interpolated curves between the data points.

of the final dropoff increases with He implantation energy because the blisters must displace progressively thicker lids. Optical microscopy on one of the samples confirmed the blistering.

V. CONCLUSIONS AND FUTURE PROSPECTS

We have used variable-energy positrons to study damage in ^4He implanted well-annealed polycrystalline Ni foils. The measured Doppler-broadened annihilation line shape versus incident-positron energy was shown to be sensitive to the damage profile generated by the ^4He ions. A semiquantitative model assuming a square defect profile was developed and fitted to the parametrized momentum data. Generally good fits were found and the width of the fitted defect distribution was in reasonable agreement with damage profiles generated from Monte Carlo results. Three different ^4He implant energies (30, 90, and 180 keV) were experimentally investigated and compared to the theory.

The ^4He fluences used were relatively high, causing saturation of positron trapping. As expected, this is responsible for the high uncertainty in determining the trapping rate K . It also means that positrons are trapped with high probability out into the tails of the He distribution, making the distribution seem less well defined. Therefore experiments with lower fluences should be carried out in the future. The square defect distribution might be a reasonable first-order approximation at high fluences. At lower fluences, however, more realistic defect distributions should be used.

Annealing studies observed changes that occurred in the microstructure during annealing. From these results it was clear that more open-volume defects (i.e., He-filled

voids) were formed at annealing temperatures above 700°C in all of the samples. These spectra were also fitted with the model and only small changes were detected in the width of defect profile, even though the nature of the positron traps changed. These variable-energy positron-annihilation results were in good agreement with He-desorption measurements of Jäger and Roth.²⁹

Specimen with square damage distribution can be prepared by He implantation with multiple energies or by implanting He at a higher specimen temperature, as demonstrated by Jäger and Roth.²⁹ Analysis of experimental data from these irradiated samples should provide more conclusive results. Furthermore, to reduce the coupling between the parameters, one can impose another constraint on Eqs. (20) and (21) by performing parallel measurements of the positronium fraction formed at the surface. This quantity is proportional to the surface fraction F_s and the proportional constant can be determined from the combined measurements for the reference sample. In practice, the defect distribution is the desired result in these studies. In the present study F_s was found to be small owing to surface contamination. Solving $K(X)$ from Eq. (11) is mathematically difficult. One of the methods involves iterative procedures which is being presently used by van Veen *et al.*³¹

The positron technique relies on specific knowledge of the positron-implantation profile. At the present time this implantation profile needs to be determined more accurately so that the depth-resolving capabilities can be further exploited. It should be noted that the depth-resolving capabilities of this technique will be much greater at low energies owing to the sharpness of the profile [see Fig. 5(a)]. Since the local positron density is higher at low incident energies, there will be a higher sensitivity to defects in resolution for profiling. More recent results³² on ^4He irradiation show that the positron technique is sensitive to ^4He fluences down to 2×10^{13} ^4He atoms/cm² with an implantation energy of 3 keV. Recently, the positron technique has been used in depth profiling of defects created by Ar irradiation of Al.³³

In the present study we have limited ourselves to mainly using the Doppler-broadening signal. Both the positronium and positron reemitted fraction and positron-lifetime measurements could have provided complementary information to the data presented here. This would be especially true in attempting to resolve the specific types and concentration of defects present in the samples.

The trapping of positrons by He bubbles which has been investigated in the present work has significant implications for the hydrogen trapping which has previously been observed in He-implanted Ni. In the hydrogen experiments,²⁶ the trapping in the presence of the He was substantially stronger than the binding to implantation damage alone. It was proposed that the hydrogen is trapped at the bubble walls by a process similar to surface chemisorption, despite He densities believed to exceed 10^{23} atoms/cm². There is strong evidence from the annealing results of the present work that the positrons were, in fact, trapped at the He bubbles, and since the measured line-shape parameter S was close to the value for the metal surface, it is believed to reflect a positron surface state at

the bubble wall. This then appears to support the earlier hypothesis that hydrogen chemisorption at the bubble walls is possible even in the presence of the high He densities. The S parameter did not conform precisely to that for a free surface or large, empty void; however, annealing produced enlargement and a reduction of the He density. This suggests that there may, in fact, be an appreciable difference between the binding enthalpy of hydrogen to the small, high-pressure He bubbles and the binding to surface sites, one which might be revealed by a more sensitive and direct experimental comparison of the two quantities.

ACKNOWLEDGMENTS

We wish to thank M. Carroll for technical assistance, Ed Traboulsi for the running of the computer programs, and A. van Veen, L. Snead, and W. R. Wampler for discussions. Work performed at Brookhaven National Laboratory is supported by the Division of Materials Sciences, U.S. Department of Energy, under Contract No. DE-AC02-76CH00016, and by the National Science Foundation under Grant No. DMR-83-15691 at Sandia National Laboratories, which is supported by the U.S. Department of Energy under Contract No. DE-AC04-76DP00789.

APPENDIX

The one-dimensional diffusion Eq. (11) together with the boundary condition Eq. (15) and a square trapping distribution Eq. (19) leads to the following solution:

$$n(x) = \frac{l'}{D_+} \frac{a \sinh(x/l)}{\sinh(x_1/l)} + \frac{l}{D_+} \int_0^{x_1} \frac{\sinh[(x_1 - x_>)/l] \sinh(x_</l)}{\sinh(x_1/l)} p(x') dx', \quad 0 \leq x \leq x_1, \quad (\text{A1a})$$

$$n(x) = \frac{l'}{D_+} \frac{\{a \sinh[(x_2 - x)/l'] + b \sinh[(x - x_1)/l']\}}{\sinh[(x_2 - x_1)/l']} + \frac{l'}{D_+} \int_{x_1}^{x_2} \frac{\sinh[(x_2 - x_>)/l'] \sinh[(x_< - x_1)/l']}{\sinh[(x_2 - x_1)/l']} p(x') dx', \quad x_1 \leq x \leq x_2, \quad (\text{A1b})$$

$$n(x) = \frac{l'}{D_+} b e^{-(x-x_2)/l} + \frac{l}{D_+} \int_{x_2}^{\infty} e^{-(x_> - x_2)/l} \sinh\left[\frac{x_< - x_2}{l}\right] p(x') dx', \quad x_2 \leq x \leq \infty. \quad (\text{A1c})$$

Therefore, from Eqs. (12) and (13),

$$F_s = \frac{1}{\sinh(x_1/l)} \left[\frac{l'a}{l} + \int_0^{x_1} \sinh\left[\frac{x_1 - x'}{l}\right] p(x') dx' \right], \quad (\text{A2})$$

$$F_d = \frac{K/(K+\lambda)}{\sinh[(x_2 - x_1)/l']} \left\{ (a+b) \left[\cosh\left[\frac{x_2 - x_1}{l'}\right] - 1 \right] + \frac{1}{l'} \int_{x_1}^{x_2} \sinh\left[\frac{x_2 - x_>}{l'}\right] \sinh\left[\frac{x_< - x_1}{l'}\right] p(x') dx' dx \right\}, \quad (\text{A3})$$

where

$$l = (D_+/\lambda)^{1/2}, \quad l' = [D_+/(K+\lambda)]^{1/2}, \quad (\text{A4})$$

$$x_> = \max\{x, x'\}, \quad x_< = \min\{x, x'\}. \quad (\text{A5})$$

The coefficients a and b are determined by the flux continuity at x_1 and x_2 , i.e.,

$$\frac{\partial n}{\partial x} \Big|_{x=x_1-\epsilon} = \frac{\partial n}{\partial x} \Big|_{x=x_1+\epsilon} = \frac{\partial n}{\partial x} \Big|_{x=x_2+\epsilon} = \frac{\partial n}{\partial x} \Big|_{x=x_2-\epsilon}, \quad (\text{A6})$$

which results in

$$a = \frac{\gamma_1 \beta + \gamma_2}{\alpha \beta - 1}, \quad b = \frac{\gamma_2 \alpha + \gamma_1}{\alpha \beta - 1}, \quad (\text{A7})$$

where

$$\alpha = \left[\frac{l'}{l} \coth\left[\frac{x_1}{l}\right] + \coth\left[\frac{x_2 - x_1}{l'}\right] \right] \sinh\left[\frac{x_2 - x_1}{l'}\right], \quad (\text{A8})$$

$$\beta = \left[\frac{l'}{l} + \coth\left[\frac{x_2 - x_1}{l'}\right] \right] \sinh\left[\frac{x_2 - x_1}{l'}\right], \quad (\text{A9})$$

$$\gamma_1 = \frac{\sinh[(x_2 - x_1)/l']}{\sinh(x_1/l)} \int_0^{x_1} \sinh(x'/l) p(x') dx' + \int_{x_1}^{x_2} \sinh\left[\frac{x_2 - x'}{l'}\right] p(x') dx', \quad (\text{A10})$$

$$\gamma_2 = \sinh \left[\frac{x_2 - x_1}{l'} \right] \int_{x_2}^{\infty} e^{-(x' - x_2)/l} p(x') dx' + \int_{x_1}^{x_2} \sinh \left[\frac{x' - x_1}{l'} \right] p(x') dx'. \quad (\text{A11})$$

To obtain the final expressions, the explicit form of the positron-implantation profile (17) with $m = 2$ was substituted for all the $p(x)$ and the integrals were given as:

$$F_s = \frac{l'a/l}{\sinh(x_1/l)} + 1 - \frac{x_0}{2l \sinh(x_1/l)} [e^{x_1/l} G(x_0, -l, 0, x_1) + e^{-x_1/l} G(x_0, l, 0, x_1)], \quad (\text{A12})$$

$$F_s^{(0)} = 1 - \sqrt{\pi} \gamma e^{\gamma^2} [1 - \text{erf}(\gamma)], \quad \gamma = \frac{1}{\sqrt{\pi}} \left[\frac{E}{E_0} \right]^n = \frac{x_0}{2l}, \quad (\text{A13})$$

$$F_d = \frac{K}{K + \lambda} \left[(a + b) \tanh \left[\frac{x_2 - x_1}{2l'} \right] + \frac{I}{\sinh[(x_2 - x_1)/l']} \right], \quad (\text{A14})$$

where a , b , α , and β are still defined by (A7)–(A9) and

$$\gamma_1 = \frac{1}{2} \left[\frac{x_0}{l} \frac{\sinh[(x_2 - x_1)/l']}{\sinh(x_1/l)} [G(x_0, l, 0, x_1) + G(x_0, -l, 0, x_1)] - \frac{x_0}{l'} [e^{x_2/l'} G(x_0, -l', x_1, x_2) + e^{-x_2/l'} G(x_0, l', x_1, x_2)] \right], \quad (\text{A15})$$

$$\gamma_2 = \frac{1}{2} \left[-\frac{x_0}{l} x_0 \sqrt{\pi} \sinh \left[\frac{x_2 - x_1}{l'} \right] e^{(x_0/2l)^2} e^{x_2/l} \text{erfc} \left[\frac{x_2}{x_0} + \frac{x_0}{2l} \right] + \frac{x_0}{l} [e^{-x_1/l'} G(x_0, l', x_1, x_2) + e^{x_1/l'} G(x_0, -l', x_1, x_2)] \right], \quad (\text{A16})$$

$$I = \frac{x_0}{2l'^2} \int_{x_1}^{x_2} dx \left[\sinh \left[\frac{x_2 - x}{l'} \right] [e^{-x_1/l'} G(x_0, l', x_1, x) + e^{x_1/l'} G(x_0, -l', x_1, x)] - \sinh \left[\frac{x - x_1}{l'} \right] [e^{-x_2/l'} G(x_0, l', x, x_2) + e^{x_2/l'} G(x_0, -l', x, x_2)] \right], \quad (\text{A17})$$

$$G(x_0, l, x_1, x_2) = \frac{\sqrt{\pi}}{2} x_0 e^{x_0/2l} \left[\text{sgn} \left[\frac{x_2 - x_0}{x_0} - \frac{x_0}{2l} \right] \text{erf} \left[\left| \frac{x_2 - x_0}{x_0} - \frac{x_0}{2l} \right| \right] - \text{sgn} \left[\frac{x_1 - x_0}{x_0} - \frac{x_0}{2l} \right] \text{erf} \left[\left| \frac{x_1 - x_0}{x_0} - \frac{x_0}{2l} \right| \right] \right]. \quad (\text{A18})$$

While the error function is well tabulated, the integral (A17) should be carried out numerically.

The parallel expression of (A13) for the exponential (i.e., $m = 1$) positron-implantation profile is

$$F_s^{(0)} = \frac{1}{1 + (E/E_0)^n}. \quad (\text{A19})$$

¹P. J. Schultz, K. G. Lynn, W. E. Frieze, and A. Vehanen, *Phys. Rev. B* **27**, 6626 (1983).

²G. Kögel and W. Triftshäuser, *Radiat. Eff.* **78**, 221 (1983).

³W. Jäger, R. Manzke, H. Trinkaus, G. Crecelius, R. Zeller, J. Fink, and H. L. Bay, *J. Nucl. Mater.* **111&112**, 674 (1982).

⁴W. D. Wilson, C. L. Bisson, and M. I. Baskes, *Phys. Rev. B* **24**, 5616 (1981).

⁵*Positrons in Solids*, Vol. 12 of *Topics in Current Physics*, edited by P. Hautojärvi (Springer-Verlag, Berlin, 1979).

⁶C. H. Hodges, *Phys. Rev. Lett.* **25**, 284 (1970).

⁷P. Hautojärvi, J. Heinio, M. Manninen, and R. Nieminen, *Philos. Mag.* **34**, 973 (1977).

⁸S. Valkealahti and R. M. Nieminen, *Appl. Phys. A* **32**, 95 (1983); **35**, 51 (1984).

⁹K. G. Lynn, *Phys. Rev. Lett.* **43**, 391 (1979).

¹⁰A. P. Mills, *Solid State Commun.* **34**, 623 (1979).

¹¹A. Vehanen, K. G. Lynn, P. J. Schultz, and M. E. Eldrup, *Appl. Phys.* **32**, 163 (1983).

¹²K. G. Lynn and H. Lutz, *Rev. Sci. Instrum.* **51**, 977 (1980).

¹³Rigorously, the first term in Eq. (2) should be split into two parts, annihilation from the surface state and from the emitted Ps atom: $F_s S_s = \Theta F_s S_{SS} + \sigma(1 - \Theta) F_s S_{ps}$, where Θ is the branching ratio and σ is introduced to account for the fact that ortho-Ps decays via three photons, of which only a fraction have energies around 511 keV and thus contribute to the measured signal. S_{SS} and S_{ps} are the line-shape parameters for positrons annihilating trapped at the surface, respectively, as Ps. Both Θ and σ can be determined from the P_s fraction measurement (Refs. 9 and 10). Θ is dependent on material as well as its surface condition. $0.25 \leq \sigma < 1$ since $\frac{1}{4}$ of the Ps

atoms formed at the surface are assumed to be singlet. With our detector resolution, σ was found to be 0.45, and typically Θ is around 50%, but in the present experiment it was made larger. This leads to a more precise definition of S_s :

$$S_s = \Theta S_{ss} + \sigma(1 - \Theta)S_{ps}.$$

- ¹⁴A. P. Mills, Jr. and C. A. Murray, *Appl. Phys.* **21**, 323 (1980).
¹⁵K. G. Lynn and D. O. Welch, *Phys. Rev. B* **22**, 99 (1980).
¹⁶B. Bergersen, E. Pajanne, P. Kubica, M. J. Stott, and C. H. Hodges, *Solid State Commun.* **15**, 1377 (1974).
¹⁷K. G. Lynn, C. L. Snead, and J. J. Hurst, *J. Phys. F* **10**, 1753 (1980).
¹⁸P. R. Bevington, *Data Reduction and Error Analysis* (McGraw-Hill, New York, 1969).
¹⁹B. Nielsen, K. G. Lynn, A. Vehanen, and P. J. Schultz, *Phys. Rev. B* **32**, 2296 (1985).
²⁰R. W. Siegel, in *Positron Annihilation*, edited by P. Coleman, S. Sharma, and L. M. Diana (North-Holland, Amsterdam, 1982).
²¹J. P. Biersack and L. G. Haggmark, *Nucl. Instrum. Methods* **174**, 257 (1980).
²²F. Besenbacher, J. Böttiger, and S. M. Myers, *J. Appl. Phys.* **53**, 3547 (1982).
²³H. E. Hansen, H. Rajainmäki, R. Talja, M. D. Bentzon, R. M. Nieminen, and K. Petersen, *J. Phys. F* **15**, 1 (1985).
²⁴A. van Veen, W. Th. M. Buters, G. J. Van der Kolk, L. M. Caspers, and T. R. Armstrong, *Nucl. Instrum. Methods* **194**, 485 (1982).
²⁵A. van Veen, W. Th. M. Buters, T. R. Armstrong, B. Nielsen, K. T. Westerduin, L. M. Caspers, and J. Th. M. De Hosson, *Nucl. Instrum. Methods* **209**, 1055 (1983).
²⁶S. M. Myers, W. R. Wampler, F. Besenbacher, S. L. Robinson, and N. R. Moody, *Mater. Sci. Eng.* **69**, 397 (1985).
²⁷W. Wycisk and M. Feller-Kniepmeier, *Phys. Status Solidi A* **37**, 103 (1976).
²⁸G. Dlubek, O. Brummer, N. Meyendorf, P. Hautojärvi, A. Vehanen, and J. Yli-Kauppila, *J. Phys. F* **xx**, 1961 (1979).
²⁹W. Jäger and J. Roth, *J. Nucl. Mater.* **93&94**, 756 (1980); *Nucl. Instrum. Methods* **182&183**, 975 (1981).
³⁰See, for example, R. N. West, in *Positrons in Solids*, Ref. 5.
³¹A. van Veen, B. Nielsen, and K. G. Lynn (unpublished).
³²B. Nielsen, A. van Veen, and K. G. Lynn, *Proceedings of the Seventh International Conference on Positron Annihilation* (World-Scientific, Singapore, 1985).
³³A. Vehanen, J. Mäkinen, P. Hautojärvi, H. Huomo, J. Lahtinen, R. M. Nieminen, and S. Valkealahti, *Phys. Rev. B* **32**, 7561 (1985).